Available online at www.sciencedirect.com
SCIENCE DIRECT®
International Journal of Heat and Mass Transfer 48 (2005) 1425–1438
International Journal of HEAT and MASS TRANSFER
www.elsevier.com/locate/ijhmt

Single nozzle spray cooling heat transfer mechanisms

Bohumil Horacek, Kenneth T. Kiger, Jungho Kim *

Department of Mechanical Engineering, University of Maryland, College Park, MD 20742, United States

Received 1 September 2004; received in revised form 29 October 2004
Available online 19 December 2004

Abstract

An investigation into single nozzle spray cooling heat transfer mechanisms with varying amounts of dissolved gas was performed using two powerful techniques. Time and space resolved heat transfer distributions produced by a single nozzle were measured using an array of individually controlled microheaters, while visualization and measurements of the liquid–solid contact area and the three-phase contact line length were made using a total internal reflectance technique. The presence of dissolved gas increased the effective subcooling of the liquid, and shifted the spray cooling curves to higher wall temperatures, but CHF was also increased. The phase-change heat transfer contribution was found to correlate directly with the contact line length for the experimental conditions tested.

Keywords: Spray cooling; Microheater array; Electronic cooling; Contact line; CHF

1. Introduction

Spray cooling occurs when liquid is forced through a small orifice, shattering into a dispersion of fine droplets which then impact a heated surface. The droplets can spread on the surface and evaporate, removing large amounts of energy at low temperatures due to the latent heat of evaporation in addition to substantial convection effects. Heat transfer rates much higher than can be attained in pool boiling are possible with sprays since there is less resistance to the removal of vapor from the heated surface. Other advantages include the possibility uniformly cooling large surfaces, low droplet impact velocity, and small temperature overshoot. Spray cooling is very complex, however, due to its dependence on many factors such as droplet size distribution, droplet velocity and impact angle, droplet number density, surface roughness, gas content, heat flux, and heater surface orientation, making it difficult to determine the dominant mechanism by which heat is removed from a wall. Numerous spray cooling heat transfer mechanisms have been proposed. At lower superheats, heat transfer occurs primarily through single-phase convection. Droplet impingement onto the liquid film can provide significant agitation, increasing the amount of heat transferred. As the superheat is increased, phase change becomes important. One proposed mechanism is by means of thin film evaporation [1] where the spray is believed to form a thin liquid layer on the heated surface through which heat is conducted. Because the top of the film is assumed to be at the saturation temperature, thinner films result in higher heat transfer as a result of the increased thermal gradient across the film. Another proposed mechanism is secondary nucleation [2,3]. Here, the impacting liquid droplets are believed to entrain vapor and/or gas into the

* Corresponding author. Tel.: +1 301 405 5437; fax: +1 301 314 9477.
E-mail addresses: horacek@web.de (B. Horacek), kkiger@umd.edu (K.T. Kiger), kimjh@umd.edu (J. Kim).

0017-9310/$ - see front matter © 2004 Elsevier Ltd. All rights reserved.
doi:10.1016/j.ijheatmasstransfer.2004.10.026

Nomenclature

C_g	gas concentration
CHF	critical (maximum before dryout) heat flux [W/m^2]
d_{32}	sauter mean diameter [m]
d_0	spray nozzle diameter [m]
$f\#$	f-number; as given by the ratio of an imaging len's focal length to clear aperture
$G_{i,j}$	normalized gray value of a single pixel at position (i,j) in a 2-D image
$G_{\min,j}$	minimum of (the smallest gray value along jth row) or 0.45
$G_{\max,j}$	maximum of (the largest gray value along jth row) or 0.65
H	Henry's constant
L_c	contact line length [m]
n	index of refraction
P	pressure
$\dot{q}''$	heat flux [W/m^2]
Re	Reynolds number
T	temperature
T_*	limiting temperature for a superheated liquid [°C]
v	velocity [m/s] or specific volume [m^3/kg]
We	Weber number

Greek symbols

Δ	difference
μ	dynamic viscosity [Pa s]
θ	included spray angle
ρ	density [kg/m^3]
σ	Surface tension [N/m]

Subscripts and superscripts

a	ambient conditions
c	critical conditions
f	property of liquid spray exiting the nozzle
fg	difference of property between vapor and liquid state
g	vapor property
i	index in x-direction
j	index in y-direction
r	reduced properties
raw	uncorrected measurement value
res	property of fluid in reservoir
sat	property at saturation conditions
sc	correction for substrate conduction losses
spray	contribution towards spray
sub	subcooled condition
tot	total
w	property at wall (surface)

liquid film, seeding nucleation sites and causing vigorous boiling within the film. The droplets can also puncture the rapidly growing bubbles, increasing the bubble nucleation frequency and the heat transfer.

Relatively little research has been performed regarding the effects of dissolved gas on spray cooling heat transfer. The authors are aware of only three studies that address this issue. The first study [4] determined that the presence of a non-condensable gas degraded condenser performance to the point where excess fluid removal was inhibited. It was noted that for fixed volume systems, the presence of gas would cause the boiling temperature to increase, increasing the surface temperature. However, a more recent study [5] has indicated that while dissolved gas indeed degrades the performance at lower wall temperatures, the maximum heat transfer is increased compared to sprays without dissolved gas. The two main effects of dissolved gas on sprays were to shift the spray cooling curves to higher temperatures and to increase CHF.

Insight into why dissolved gas increases heat transfer can be obtained from single droplet studies. A previous study has shown that dissolved gases and solid precipitates can increase droplet heat transfer [6]. Carbon dioxide gas or a salt was dissolved in water and videos of the evaporation process were obtained as the droplets struck a heated surface. For temperatures below and above the boiling point, the dissolved gas (0.74 mm^3/mm^3) was observed to increase the heat transfer slightly due to an increase in the splat circumference. When 1% by weight of $NaHCO_3$ was added to the liquid, it decayed when heated into Na_2CO_3 and CO_2. Foaming within the droplet occured along with a large increase in heat transfer. Precipitation of Na_2CO_3 salt within the drop served as nucleation sites for boiling, and the CO_2 produced caused the droplet to swell, increasing the contact area. Another study investigated heat transfer under drops impacting a constant-temperature surface in which bubbles formed due to dissolved gas coming out of solution [7]. In some cases, a large bubble formed within the drop and burst during the evaporation process. Formation of larger bubbles within the drop was found to increase the wall heat transfer and decrease the drop lifetime. The wall heat transfer due to an evaporating drop was found to be primarily dependent on the liquid–vapor contact area and not the liquid–solid contact area, indicating that the vapor removal process was the limiting thermal resistance.

Uncertainty regarding spray cooling heat transfer mechanisms is primarily due to difficulties in obtaining local measurements of the heat transfer and observing the state of the liquid on the surface. In this paper, we

examine single nozzle spray cooling heat transfer mechanisms using two powerful techniques. A microheater array in conjunction with electronic feedback circuits is used to measure the heat transfer distribution on a surface that is nominally uniform in temperature, simulating a thick surface with high thermal conductivity. Simultaneously, a total internal reflection (TIR) technique is used to observe the liquid on the surface and image processing is used to determine the wetted area fraction and the contact line length density (CLL). Measurements were obtained with the nozzle spaced 17 mm normal to the surface with varying amounts of dissolved gas.

2. Experimental apparatus

A full cone ISR spray nozzle was used to cool a microheater array with total area of 0.49 cm^2 (7.0 mm × 7.0 mm). The array consisted of 96 heaters each nominally 700 μm in size, similar to that used in a previous study [7]. A picture of the array is shown in Fig. 1, along with a schematic showing the heater numbering and the location of inoperable heater elements that occurred during the fabrication process. Each heater element consisted of a thin (200 nm thick, 7 μm wide) serpentine platinum resistance heater than was sputtered onto a tungsten adhesion layer on the 500 μm thick fused silica substrate. The effective temperature coefficient of resistance of the metallic layer was approximately 0.002 $°C^{-1}$, and the length, width, and thickness of the serpentine elements were designed to provide a nominal resistance of approximately 180 Ω. Thicker gold leads were deposited up to the edge of the array to ensure minimal lead resistance (<1 Ω), and the entire array was covered with a 1 μm SiO_2 passivation layer to provide a uniform surface energy.

Individual heater elements were maintained at a constant specified temperature through the use of 96 separate Wheatstone bridge feedback circuits, one of which is illustrated schematically in Fig. 2. The temperature of the element was selected through the use of a 20 kΩ digital potentiometer with 512 discrete steps. When combined with the other resistor elements in the circuit, this provided for an effective temperature regulation range from 30 °C to 110 °C with a resolution of approximately 0.2 °C. In the current configuration, each heater is capable of dissipating 1.3 W, or a maximum surface heat flux of up to 250 W/cm^2. The settings for the digital potentiometer were calibrated through the use of an insulated, constant-temperature, calibration oven. A feedback controller was used to maintain a constant interior oven temperature, while the threshold setting of the digital potentiometer that just started regulation of the circuit was determined. The calibration was performed on each of the heater elements in 5 °C increments between 30 °C and 100 °C. During the experiments, two 64-channel 12-bit analog-to-digital conversion boards were used to sample data from each individual heater at 1000 Hz.

Use of a transparent silica substrate combined with the 50% coverage area of the serpentine heater element allowed for visualization of the impacting spray by looking through the silica substrate. A high-speed digital camera (Vision Research Phantom v4.0) capable of acquiring 512 × 512 pixel images at speeds up to 1000 fps was used to record the images. The camera was configured to run with a reduced sensor size of 128 × 512 pixels, operating at 1000 fps, and was synchronized to the data acquisition system of the heater array. A tele-microscope lens (Infinity KC with IF3

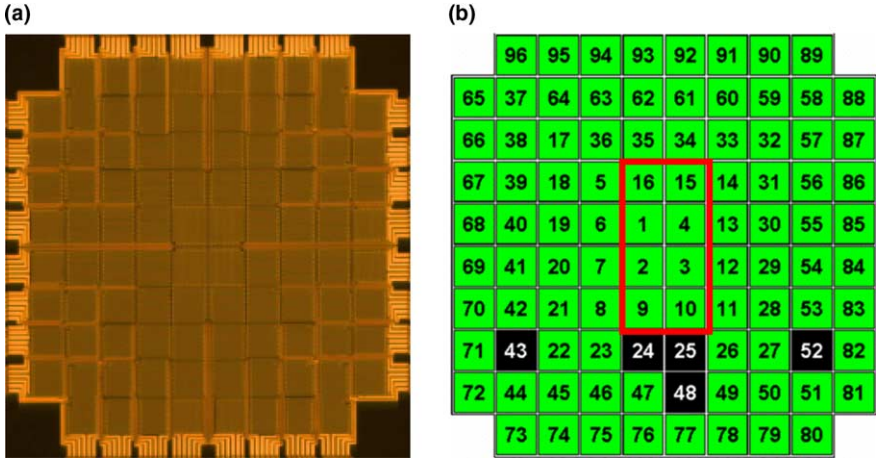

Fig. 1. Photograph of heater array (a) and schematic of heater numbering (b). Inoperable heaters (24, 25, 43, 48, and 52) are indicated in black.

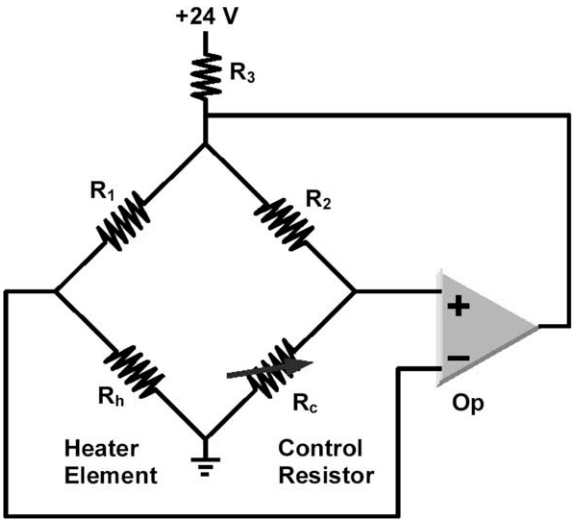

Fig. 2. Schematic of feedback control circuit for individual heater element.

objective) provided variable magnification imaging (0.9X–1.3X) with a working distance of 15 cm to 19 cm. The lens and camera were adjusted to provide a clear image of 8 heaters in a 2×4 formation on the array surface (heaters marked numbers 1, 2, 3, 4, 9, 10, 15, 16 in Fig. 1). Areas of liquid–solid contact area were obtained using the total internal reflection (TIR) technique shown schematically in Fig. 3. A right angle prism (index of refraction, $n = 1.517$) was placed in contact with the underside of the silica substrate ($n = 1.544$) containing the heater array. An optical immersion oil ($n = 1.52$) ensured no air gap existed between the prism and the substrate. Light from a collimated source was then positioned such that total internal reflection of the light occurred at the interface between the SiO_2 passivation layer ($n = 1.46$) and the vapor in the chamber ($n = 1.00$), resulting in a bright area on the image (see ray trace (a) in Fig. 3). The critical angle for total internal reflection from SiO_2 to a vapor is approximately 43°, which conveniently allowed the use of a 45° prism to direct the light onto the substrate. If liquid was present, then the light traveled past the liquid/SiO_2 interface and was scattered at the liquid–air interface, forming a dark region on the image. A small percentage of light was reflected directly from the SiO_2/liquid interface, but calculations showed this to be less than 4% of the incident light. Due to the relatively small aperture and long working distance of the lens ($f\# \sim 10$), light that was scattered at the liquid/vapor interface but was not parallel to the lens axis was not imaged. The only exception to this was at locations where the slope of the interface was nearly parallel to the SiO_2 surface. For the small surface features observed under most conditions, these points were typically confined to regions below the resolution of the camera. An example of the type of image that could be obtained is shown in Fig. 4, under conditions where the wall temperature was close to CHF. The dark areas indicate liquid on the surface. The heater area covered by liquid and the length of the three-phase contact line could easily be determined with appropriate image processing (discussed below). The TIR technique has been used in the past to study droplet impact [8] and pool boiling [9,10].

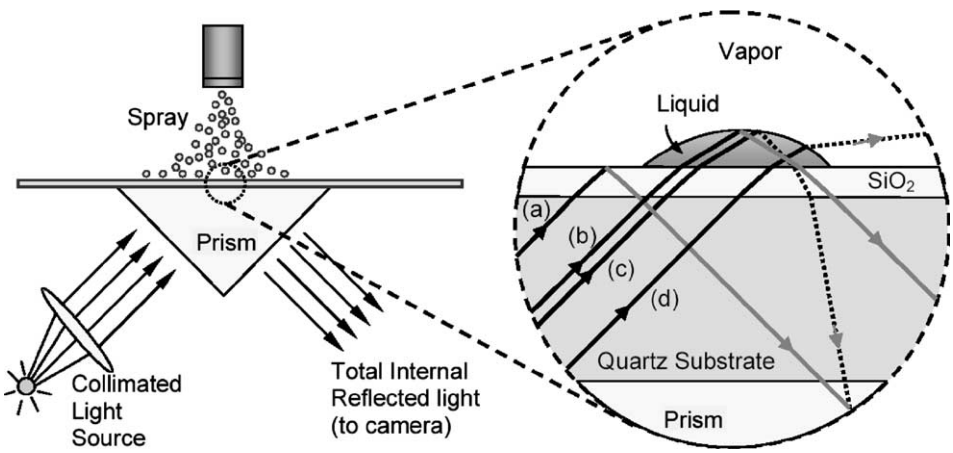

Fig. 3. Schematic of total internal reflectance (TIR) technique. Light incident at the SiO_2/vapor interface (a) undergoes a total internal reflection, while light incident on the SiO_2/liquid interface is transmitted (b–d). Most of the light (96%) striking the liquid/vapor interface is transmitted into the liquid and subsequently is scattered by a combination of reflection at a sloped interface (c) or refraction into the vapor (d). Places where the liquid surface is completely parallel to the SiO_2 surface will reflect the light to the camera, but these are typically confined to regions smaller than the image resolution.

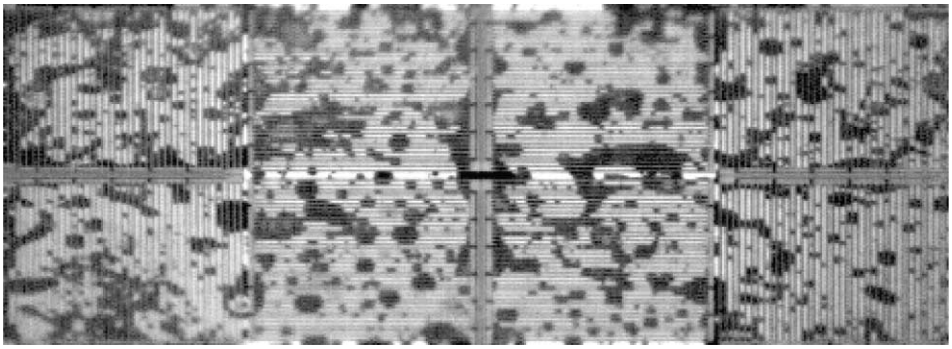

Fig. 4. Sample image obtained using the total internal reflection technique.

The tests were performed within a closed flow loop consisting of a spray chamber, condenser, and pump (see schematic in Fig. 5) with FC-72 as the test fluid. The FC-72 was distilled before placing it in the flow loop, and only fluid that evaporated between 56 °C and 60 °C was used in the tests. The test section was 25 mm wide, 16 mm high, and approximately 180 mm long. Temperature and pressure measurements were made at the inlet to the spray nozzle and within the liquid reservoir. The pressure was observed to be uniform throughout the flow loop under all conditions tested. Liquid flow to the spray nozzle was measured using a rotameter. The heater array faced upward, but was inclined at a slight angle with respect to the horizontal to help excess fluid that did not vaporize drain through the condenser into the reservoir. The nozzle distance from the heater surface was fixed at 17 mm for all tests. The nozzle diameter was measured from photographs to be $d_0 = 0.2$ mm. The pump was a magnetically coupled gear pump with a head capable of pumping up to 50 ml/min. The amount of dissolved gas within the liquid was varied by controlling the pressure within the test section using a vacuum pump. A chiller consisting of a copper coil immersed in an ice bath or LN_2 bath was used in some cases to cool the liquid entering the spray nozzle. A summary of the test procedure is as follows:

(1) The total system pressure was adjusted by removing air/vapor mixture with a vacuum pump or adding air from a pressurized tank. The spray was operated continuously to circulate the fluid until the desired equilibrium system pressure was established, and the system was then sealed.
(2) The temperature of the fluid entering the nozzle was set.

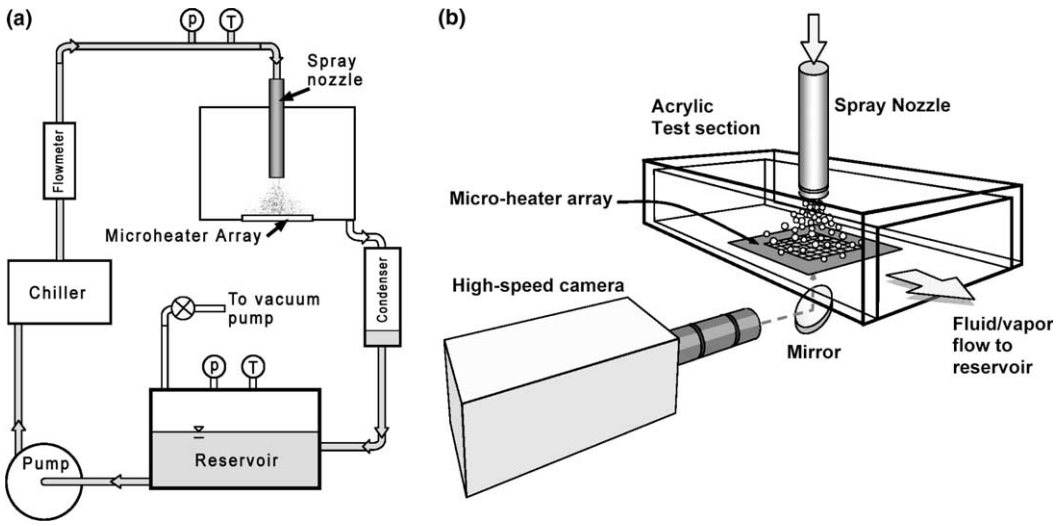

Fig. 5. Test apparatus: (a) schematic of test loop facility, and (b) detail schematic of test section, spray nozzle, heater and high-speed camera.

(3) The wall temperature for the experiment was fixed, and the system was monitored to ensure a steady system pressure was maintained. The excess heat generated by the surface heater was sufficiently small such that it was dissipated by conduction and natural convection from the walls of the reservoir. Once stabilized, the data was acquired. The procedure was repeated for each wall temperature at a fixed system pressure.

The temperature of the fluid reservoir was maintained at a constant temperature of approximately 23 °C throughout all of the tests.

3. Image processing

In order to extract quantitative information from the images, the influence of the opaque heater lines must first be removed. For the magnification used in acquiring the images, the heater lines were approximately 1 pixel in width. A 2-pixel orthogonal line filter combined with a line-by-line renormalization was found to be effective in removing these unwanted features and allowed for robust identification of wetted regions. This process operated on a single heater in the array is illustrated in Fig. 6. Fig. 6a shows the original image obtained from the high-speed camera. First, a 2-pixel averaging filter was convolved with the image such that the orientation of the 2-pixel stencil was orthogonal to the heater lines. For the heater with horizontal elements shown in Fig. 6, this corresponded to a vertical stencil having each pixel averaged with the neighbor immediately above itself. The results of this filtering are shown in Fig. 6b, and has the effect of smearing out the heaters without losing significant details of the droplets. Second, each pixel element (denoted by subscript i) in the line along the direction of the heater element (denoted by the subscript j) was renormalized by the minimum and maximum values contained in that individual line:

$$\widehat{G}_{i,j} = \frac{G_{i,j} - G_{\min,j}}{G_{\max,j} - G_{\min,j}} \tag{1}$$

with $G_{\min,j} = \min[G_j, 0.45]$ and $G_{\max,j} = \max[G_j, 0.65]$. The minimum and maximum normalization values were constrained to a relative contrast of 0.45 and 0.65 (0 = black, 1 = white), respectively, to prevent lines that are not wet by any liquid (or conversely lines that are not exposed to any vapor) from being scaled to the full-scale contrast range. In the case of the heater shown in Fig. 6, the lines were taken horizontally, resulting in a more uniform grayscale range which tended to remove any residual variation caused by the presence of the heater element image (see Fig. 6c). This was also found to work well in dealing with the weak spatial non-uniformity of the illumination source and the shot-to-shot variability of the strobe intensity. The final processed image was obtained by taking a threshold grayscale value to determine the boundary between the wet and dry regions of the vapor interface, as shown in Fig. 6d. Light gray patches inside and around the liquid regions were often observed. These are believed to be regions of thin fluid where the curvature is weak relative to the thickness of the film, thus reflecting some of the light from the liquid/vapor interface. It was found that setting the threshold level to a value of 0.56 easily detected these regions as wetting liquid, while still rejecting the other dry regions of the surface. The smallest features that could be consistently detected by these means were found to be around 3–4 pixels, which corresponds to a wetted contact region of approximately 15 μm in diameter.

4. Uncertainty analysis

The instantaneous power required to keep each heater at a constant temperature was measured and used to determine the heat flux from each heater element. Because all the heaters in the array were at essentially the same temperature, heat conduction between adjacent heaters was negligible. The total heat flux measured for each heater ($\dot{q}''_{\text{raw}}$), however, must be corrected to account for substrate conduction. $\dot{q}''_{\text{raw}}$ could be lost by conduction through the substrate ($\dot{q}''_{\text{sc}}$), or to the spray ($\dot{q}''_{\text{spray}}$). $\dot{q}''_{\text{sc}}$ for each heater in the array at a set tempera-

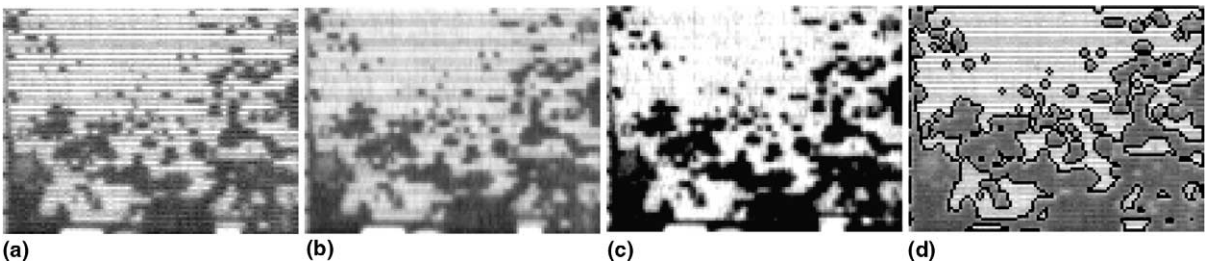

Fig. 6. Image processing sequence. From left to right (a) original image, (b) 2-pixel orthogonal filter applied, (c) line-by-line renormalization, and (d) final detected edges superimposed on original image.

ture could be determined by setting the heater to the specified temperature and measuring the power required to keep it at that temperature with no spray on the surface. The natural convection from the heater was smaller than 0.1 W/cm^2, much smaller than the measured spray cooling heat fluxes. In all of the cases studied, $\dot{q}''_{sc}$ was much smaller than $\dot{q}''_{spray}$ for all heaters except the edge heaters (heaters 65–96 in Fig. 1) since the substrate was relatively thin (450 μm) compared to the heater size (700 μm). The edge heaters acted as "guard" heaters for the internal heaters (heaters 1–64 in Fig. 1), and prevented heat loss through the substrate for the internal heaters. The heat dissipation rate for the edge heaters changed depending on convection mechanism since the heat transfer from the unheated portion of the substrate also changed. In the data discussed below, the heat transfer from the edge heaters has been excluded from the calculations.

The uncertainty in the heat flux due to measurement errors resulted from uncertainties in $\dot{q}''_{raw}$ and $\dot{q}''_{sc}$. Uncertainties in $\dot{q}''_{raw}$ were relatively small since they were computed directly from the measured voltage across the heaters and since the variation in the heater resistances was small. The maximum uncertainty in the voltage across the heater was 0.04 V. The uncertainty in heater resistance was about 1 Ω. Since the heater resistance was nominally 180 Ω, the uncertainty in heater resistance was about 0.56%. The resulting uncertainty in heat transfer due to measurement inaccuracies in the feedback circuit and data acquisition system were conservatively calculated to be less than 3%.

Larger uncertainties in the spray cooling curve could result from uncertainties in liquid flow rate, wall temperature, and dissolved gas concentration. The liquid flow rate was steady to within 0.5 ml/min (1.4–4.5% over the range of flow rates tested). The uncertainty in wall temperature was assumed to be two positions on the digital potentiometer, or 0.4 °C. The amount of gas in the flow loop was determined by measuring the pressure and temperature in the flow loop. The distribution of the gas, however, could vary within the flow loop if the temperatures varied (which is likely since the heater is hotter than the surroundings), making it difficult to quantify the local gas concentration. The accuracy of the pressure transducer used was 1.5%. Repeated measurements of the spray cooling curves under the same nominal conditions resulted in errors of about 4%. The total uncertainty in the spray cooling curves obtained by combining the uncertainty in repeatability with the measurement inaccuracies was estimated to be 5%.

5. Effect of gas

The presence of any non-condensable gas increases the pressure in the test section above the saturation pressure of the liquid corresponding to the reservoir temperature. Assuming the non-condensable gas and the liquid are in contact sufficiently long to attain equilibrium conditions, Henry's law can be used to estimate the amount of dissolved gas in the liquid. The dissolved gas concentration C_g (moles gas/mole liquid) in the liquid phase is given by

$$C_g = H(T)P_g \tag{2}$$

where P_g is the partial pressure of the gas above the liquid and $H(T)$ is Henry's constant. For air in FC-72, $H(T) = 5.4 \times 10^{-5}$ mole/mole kPa for 31 °C < T < 60 °C [11]. P_g was determined from a measurement of the pressure (P_{tot}) and temperature (T_{sat}) of the gas above the liquid after it reached equilibrium in a sealed container from the following equation:

$$P_g = P_{tot} - P_{sat}(T_{sat}) \tag{3}$$

where P_{sat} is the saturation pressure of the liquid at the measured temperature T_{sat}.

Subcooling of the liquid entering the spray nozzle could be accomplished in two ways. Consider first the case where all gas has been removed from the test section. The pressure in the flow loop is equal to the vapor pressure of the liquid in the reservoir. Liquid can be pumped from the reservoir through a chiller to decrease its temperature before being sprayed on the heater. The liquid sprayed onto the heater is now in a state we will refer to as "thermally subcooled" (TS). TS is defined as the temperature difference between the reservoir temperature and the liquid spray temperature. Consider next the case where air is allowed into the flow loop. The saturation temperature of the liquid in the reservoir has now increased since the pressure above the liquid is higher than the vapor pressure. Even if liquid from the reservoir is not cooled before entering the spray nozzle, the liquid being sprayed onto the heater will be effectively subcooled since its temperature is below the saturation temperature. The liquid sprayed onto the heater is in a state we will refer to as "gas subcooled" (GS) which is similar to the terminology used in earlier studies of gas effects on pool boiling [12], and is defined as the temperature difference between the saturation temperature and the reservoir temperature. The total subcooling (S_{tot}) is defined as

$$S_{tot} = \mathrm{TS} + \mathrm{GS} = (T_{res} - T_f) + (T_{sat} - T_f) \tag{4}$$

It is seen from the above discussion that one of the primary effects of non-condensable gas is to change the saturation temperature of the liquid, and therefore the amount by which the liquid being sprayed on the surface is subcooled for a constant spray temperature. For example, consider the case where liquid FC-72 is at 22 °C in the reservoir. If the flow loop is at 1 atm due to the presence of gas (T_{sat} = 56.6 °C) and liquid from the reservoir is sprayed onto the heater, the liquid will

be gas subcooled by GS = 34.6 °C (GS = $T_{sat} - T_f$ = 56.6 °C − 22 °C). If the gas is now completely removed from the flow loop, the liquid spray will be saturated and the pressure in the loop will be 0.26 atm. In order to match the subcooling for the 1 atm case, the liquid will need to be thermally subcooled to $T_f = -12.6$ °C ($T_f = T_{res} - TS = 22$ °C − 34.6 °C). It is possible for TS to be negative provided non-condensable gas is present in the chamber and the liquid is heated to a temperature greater than the reservoir temperature prior to ejection from the spray nozzle. The subcooled state of the liquid being sprayed onto the heater can be characterized by specifying TS and GS.

6. Results

Results were obtained with the spray nozzle oriented normal to the microheater array, with the orifice located 17 mm from the surface. The entire heater surface was covered by the spray. The flow rate through the nozzle was set at 32 ml/min, which was attained when the pressure drop across the nozzle reached 3.67 atm. The actual volumetric flux of liquid on the heater was measured by replacing the heater with an insert with a machined hole of the same size and shape as the heater array. The sides of the insert were sloped so that the liquid impacting the insert outside the hole were deflected away from the hole. With the insert spaced 17 mm from the nozzle, the flow rate impacting the heater area was measured to be 11.3 ml/min.

The spray cone angle was measured to from side view photographs of the spray to be approximately 32°. The size of the drops produced by the nozzle was estimated using a correlation for FC-72, FC-87 and water [13]:

$$\frac{d_{32}}{d_0} = 3.67[We_{d_0}^{1/2} Re_{d_0}]^{-0.259} \tag{5}$$

where $We_{d_0} = \frac{\rho_a(\frac{2\Delta P}{\rho_f})d_0}{\sigma}$, $Re_{d_0} = \frac{\rho_f(\frac{2\Delta P}{\rho_f})^{1/2}d_0}{\mu_f}$. The mean absolute error of this correlation is claimed to be 12%. d_{32} was computed from this correlation to vary from 50 μm for Cases 4 and 5 down to 38 μm for Cases 1 and 2. An estimate of the initial fluid velocity leaving the nozzle, obtained from $v = \sqrt{2\Delta P/\rho_f}$, was 21 m/s for all cases. The actual impact velocity of the droplets, however, is lower as a result of the hydrodynamic drag on the droplets and the energy lost to breaking the continuous fluid stream into discrete droplets. Limited measurements using a Phase Doppler Particle Analyzer under ambient conditions ($T_f = 23$ °C, $P_a = 1$ atm, and a flowrate of 30 ml/min) at a distance of 20 mm from the nozzle tip indicated d_{32} ranging from 40 to 50 μm (smallest size at the centerline, largest at the edges) with an axial velocity component of 3 m/s near the edges with a maximum of 6 m/s on the centerline. A summary of the test conditions is presented in Table 1. For Case 5, air was pumped into the flow loop to increase the pressure above 1 atm.

6.1. Effect of thermal subcooling on degassed fluid

Spray cooling curves showing the effect of thermal subcooling on nominally degassed fluid are shown in Fig. 7, Cases 1 and 2. The heat flux shown is the average heat flux from the center 64 heaters in the array. Thermal subcooling is seen to increase the heat transfer for

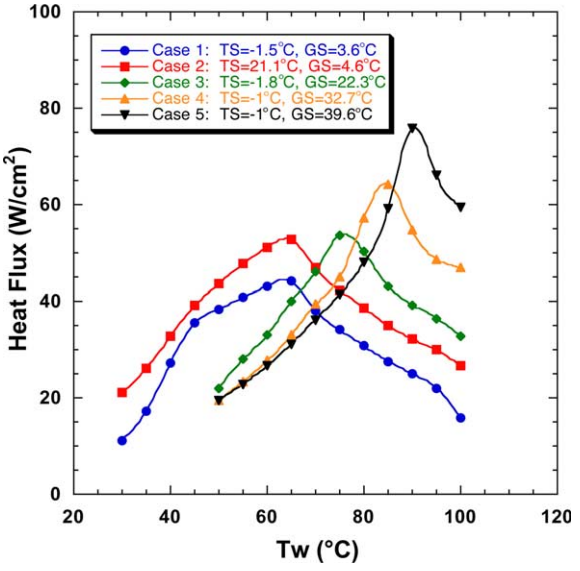

Fig. 7. Effect of thermal subcooling and dissolved gas as a function of wall temperature.

Table 1
Summary of test conditions

Case no.	T_{res} (°C)	T_{spray} (°C)	P_{res} (atm)	T_{sat} (°C)	TS (°C)	GS (°C)	Comments
1	23.5	25	0.33	27.1	−1.5	3.6	Nominally degassed, saturated liquid
2	22.5	1.4	0.33	27.1	21.1	4.6	Nominally degassed, thermal subcooling
3	23.2	25	0.67	45.5	−1.8	22.3	Gassy subcooling comparable to thermal subcooling of Case 2
4	24	25	1.0	57.6	−1	32.7	Test rig at nominally 1 atm, gassy subcooling
5	24	25	1.22	68.1	−1	39.6	Test rig above 1 atm, gassy subcooling

a given flow rate due to the sensible heating required to bring the fluid up to the saturation temperature, and is consistent with the results of previous researchers. Thermal subcooling does not affect the temperature at which CHF occurs.

6.2. Effect of dissolved gas

The effect of varying amounts of dissolved gas on spray cooling for the constant flow rate used in these experiments is also shown in Fig. 7. The spray cooling curves shift to the right and CHF increases with increasing gas content, consistent with the trends observed by Lin and Ponnappan [5]. The shift to higher temperatures is a direct consequence of the increase in T_{sat} when dissolved gas is present. As pointed out in the previous section, the increase in T_{sat} results in an effective increase in the subcooling of the liquid being sprayed onto the surface. The data for the highest gas content cases (Cases 4 and 5) merge for $T_{wall} = 50$ °C and $T_{wall} = 55$ °C as expected since the wall temperature is below the saturation temperature. Heat is primarily transferred by single-phase convective cooling in this regime, although there may be some contribution from degassing assisted evaporation, especially considering the high solubility of air in FC-72. The liquid for Case 3 strikes a wall that is slightly superheated ($T_{wall} = 50$ °C), and this is reflected in the small increase in heat transfer above the data for Cases 4 and 5. The data for Cases 1 and 2 (nominally degassed liquid) are significantly higher, indicating that evaporation plays a major role in spray cooling for these conditions.

The data in Fig. 7 was manipulated in two ways to account for the effect of changes in T_{sat} with gas content. First, the saturation temperature for each case was subtracted from the wall temperatures to obtain wall superheat on the abscissa. Second, the mass flow rate impacting the total array (11.3 ml/min) was divided by 96 to obtain the average mass flow per heater and used to calculate a sensible heat contribution to the heat flux by assuming that the liquid striking the surface is heated to the saturation temperature. The sensible heat was then subtracted from the measured heat flux to obtain a heat flux corrected for the sensible heat changes from case to case. The corrected heat flux data plotted vs. wall superheat are shown in Fig. 8. It can be observed that the large variation in CHF values in Fig. 7 of about 32 W/cm^2 has been reduced to about 15 W/cm^2 by correcting for sensible heating. Although the superheat at which CHF occurs decreases with gas content, CHF occurs within a fairly narrow range of superheats (about ±8 °C), which may be indicative of a nascent Leidenfrost-type phenomena where a thin vapor layer prevents liquid from wetting the surface. Kopchikov et al. [14] suggested that the peak heat flux during boiling within thin films occurs when the wall temperature reaches a

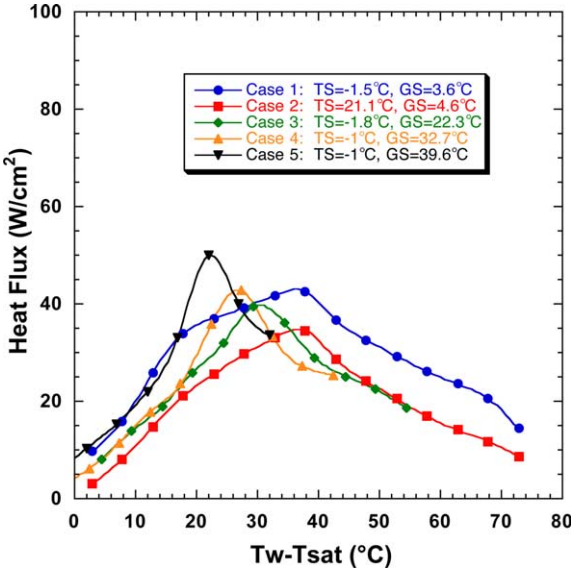

Fig. 8. Heat flux corrected for sensible heating and wall superheat.

certain fraction of the limiting superheat for a metastable liquid:

$$T_{CHF} - T_{sat} = \xi(T_* - T_{sat}) \tag{6}$$

where ξ is a coefficient that depends on the properties of the heated surface in contact with the liquid. Their measurements with water, ethanol, carbon tetrachloride, and benzene suggested $\xi = 0.83$. An estimate of the limiting temperature T_* can be obtained using the Berthelot equation of state

$$\left(P_r + \frac{3}{T_r v_r^2}\right)\left(v_r - \frac{1}{3}\right) = \frac{8}{3}T_r \tag{7}$$

along with the stability criterion $\partial P_r/\partial v_r|_{T_r} = 0$ to obtain the spinodal curve. For the cases studied (FC-72, critical temperature and pressure are 178.5 °C and 18.16 atm, respectively), the limiting temperatures were computed to be about 143 °C while ξ was between 0.29–0.33 (Table 2), suggesting that this may be a method of predicting the temperature at which CHF occurs. The reason for the difference in ξ values between the work of Kopchikov et al. [14] and the current results is not known.

Presence of a non-condensable gas is also observed to exert a significant effect on the heat transfer beyond its contribution to the sensible heat via subcooling. Comparison of Case 2 ($S_{tot} = 25.7$ °C, predominantly thermally subcooled) and Case 3 ($S_{tot} = 20.5$ °C, predominantly gas subcooled) on this figure reveals the role of gas at roughly similar S_{tot} levels. Even though S_{tot} for Case 2 is larger than S_{tot} for Case 3, higher heat transfer is generally observed for Case 3, indicating the gas has an effect in addition to the direct influence of subcooling.

Table 2
Summary of superheat limit and ξ calculation

Case no.	$P_r = P/P_c$	T_*/T_c	T_* (°C)	T_{CHF} (°C)	T_{sat} (°C)	ξ
1	0.0182	0.920	142	65	27.1	0.33
2	0.0182	0.920	142	65	27.1	0.33
3	0.0368	0.921	143	75	45.5	0.30
4	0.0552	0.922	143	85	57.6	0.32
5	0.0671	0.923	144	90	68.1	0.29

The presence of gas may cause additional single-phase convection over the heater areas not covered by drops, or can contribute to additional evaporation of the liquid. The gas may also cause bubbles to nucleate within the drops or surface film, spreading the liquid over a larger heated area thereby increasing the liquid–solid contact area or by increasing the liquid–vapor contact area and increasing the heat transfer. Similar behavior was observed in studies of dissolved salt effects on spray cooling heat transfer [15]. The increase in heat transfer with dissolved salts was attributed to an increased foaming in the thin liquid film.

A CHF correlation that accounts for volumetric flow rate, fluid properties, spray angle, droplet diameter, and subcooling has been proposed by Mudawar and Estes [16]:

$$\frac{\dot{q}''}{\rho_g h_{fg} \overline{\dot{V}}''} = 1.467[(1+\cos(\theta/2))\cos(\theta/2)]^{0.3}\left(\frac{\rho_f}{\rho_g}\right)^{0.3} \times \left[\frac{\rho_f \overline{\dot{V}}''^2 d_{32}}{\sigma}\right]^{-0.35}\left[1+0.0019\frac{\rho_f c_{p,f}\Delta T_{sub}}{\rho_g h_{fg}}\right] \quad (8)$$

Comparison of the measured CHF results to those obtained by using S_{tot} in place of ΔT_{sub} in the correlation indicates agreement within the claimed uncertainty of 30% (Fig. 9). It appears that gas effects on CHF for these results can be predicted using this correlation.

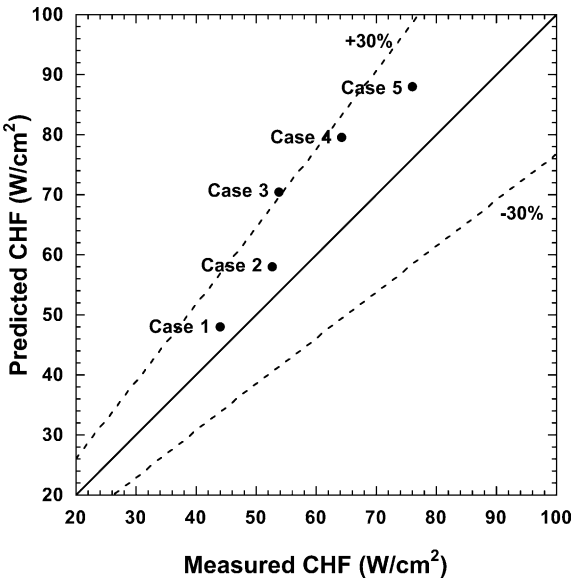

Fig. 9. Comparison of measured CHF values to those predicted by Mudawar and co-worker [13].

6.3. Visualization of flow structure

Sample images of the wetted surface using the TIR technique are shown in Fig. 10 for various non-condensable gas contents and wall superheats, and provide a qualitative representation of the wetted surface characteristics for the various conditions of the test. Examining first the case of liquid in contact with its vapor (no gas subcooling), it can be seen that the surface was almost completely wet by liquid at low wall superheats. Occasionally, several dry spots appeared, likely due to a surface perturbation from either convective film instabilities or impacting droplets. These dry spots were typically rewet in subsequent images. As the wall superheat was increased, the dry regions increased in frequency and size, eventually producing isolated pools of liquid. Within the dry regions, very fine droplets were frequently observed (less than 40 μm in diameter). As CHF was approached, very few large pools of liquid remained, leaving the heater surface largely covered by intermediate-sized droplets (typically 150 μm and smaller). Beyond CHF, a portion of the heater appeared to permanently dry out and was ringed by droplets of increasing size.

The very finest visible droplets may be a result of droplet impacts directly from the spray since the size of these droplets are of the same order of magnitude as those measured from the spray nozzle (recall that d_{32} is approximately 50 μm in diameter). The presence of intermediate-size droplets that are much bigger than the primary spray size, however, also indicates that many of these droplets are likely to be the result of the larger pools vaporizing and/or the pools dividing into smaller domains by instabilities on the pool surface. It is also possible that some of these result from coalescence of smaller spray droplets that have joined together, but this would require the vaporization lifetime

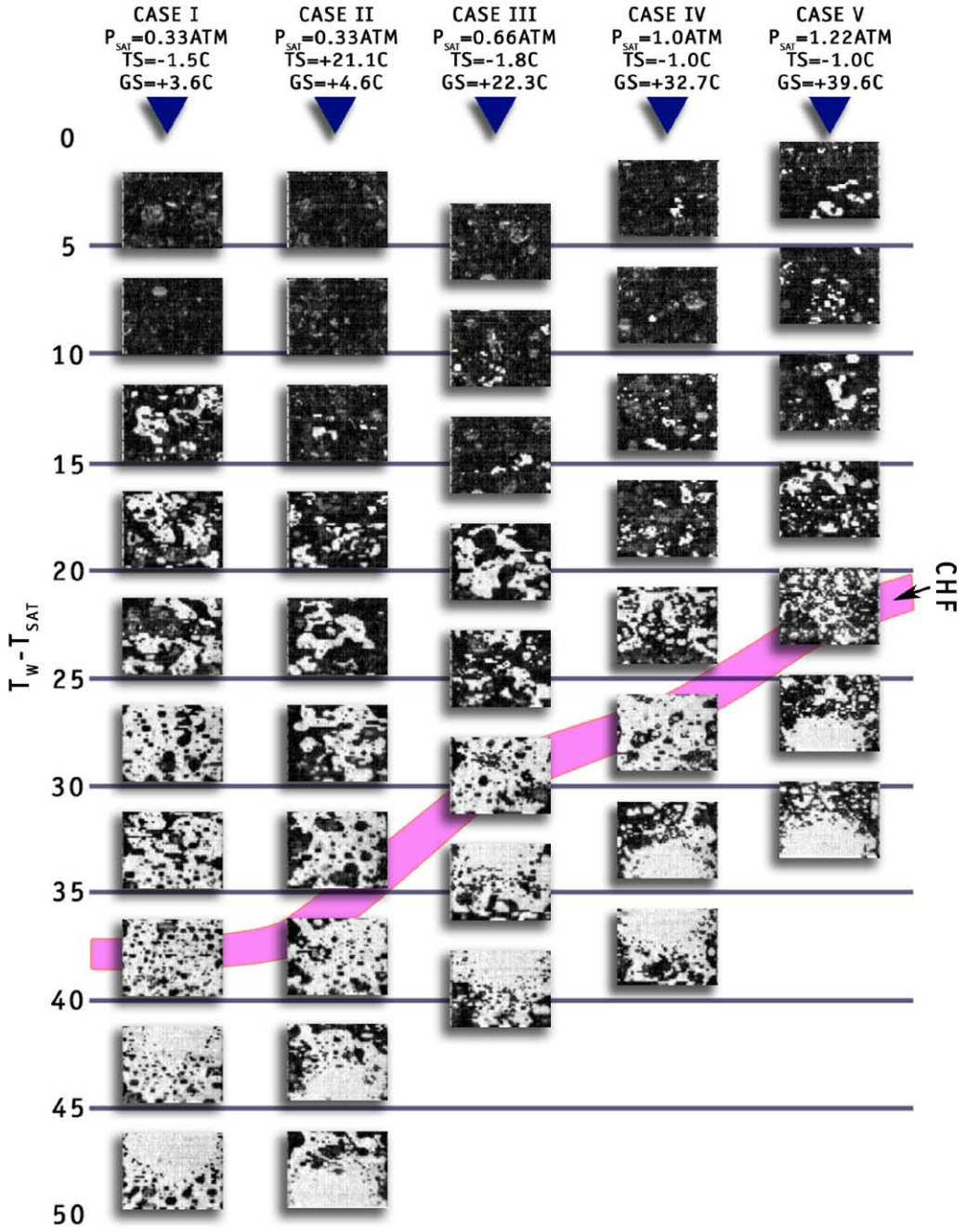

Fig. 10. Representative images of surface wetting on a single heater for various wall superheat and gas/thermal subcooling levels. The light-colored band in the background represents the approximate conditions for CHF. The temperature scale is placed to indicate the proper superheat based on the top edge of the image.

of the droplets to be large in comparison to the inter-collision time of the spray with the surface.

For increased non-condensable gas content, the intermittent dry regions at low superheats gradually increase in number (at a fixed instant in time) and occur with greater temporal frequency. This is clearly evident for Case 5 (GS = 39.6 °C). The reason for this may be a combined result of a decreased surface tension at higher wall temperatures and the mass transport of the absorbed gas escaping the liquid as it is heated. As the wall superheat was increased and CHF approached, numerous small void regions rapidly appeared within

the larger pools. Again this may have been a result of the gas trying to escape the liquid, or possibly the presence of the gas allowing the onset of nucleate boiling within the pool. It should be noted, however, that the location of the voids were not fixed but changed with each image. This observation is inconsistent with heterogeneous nucleate boiling, and indicates that the nucleation may be associated with the random droplet impacts either through the release of gas dissolved within the liquid, or small air bubbles entrained by impact of the droplet on the liquid film. TIR images of pool boiling also look different from those obtained in this study. Nishio and Tanaka [10] studied pool boiling on a sapphire substrate using ethanol, R113, and R141b. They observed isolated circular dry areas under low wall superheats conditions. At higher superheats, coalesced dry areas appeared, but "a network of liquid–solid contacts like a canal meandering between dry areas" were observed on the surface and small circular dry areas within these liquid–solid contacts could be seen. In the current spray cooling studies, no such "canals" between dry patches were observed.

Statistical quantification of the images was possible through the identification of various geometrical characteristics of the wetted surface, such as the wetted area fraction and the contact line length density (CLL). Fig. 11 shows the average fraction of the heater surface wet by liquid as a function of wall superheat, and indicates that the wetted area fraction monotonically decreases as the wall superheat increases, independent of both TS and GS. The amount of liquid on the surface appears to correlate with wall superheat and not with heat flux. If CHF is taken to occur at an average superheat of 30 °C, the corresponding wetted area fraction is about 0.45. This is close to the wetted area fraction of 0.40 at CHF obtained in Nishio and Tanaka's [10] pool boiling study. It should be noted, however, that the variation of wetted area changes rapidly with superheat near CHF, and the actual values of the wetted area fraction vary from 0.31 for the nominally degassed conditions (Case I, $T_{w,CHF} - T_{sat} = 37.8$ °C) to 0.65 for the

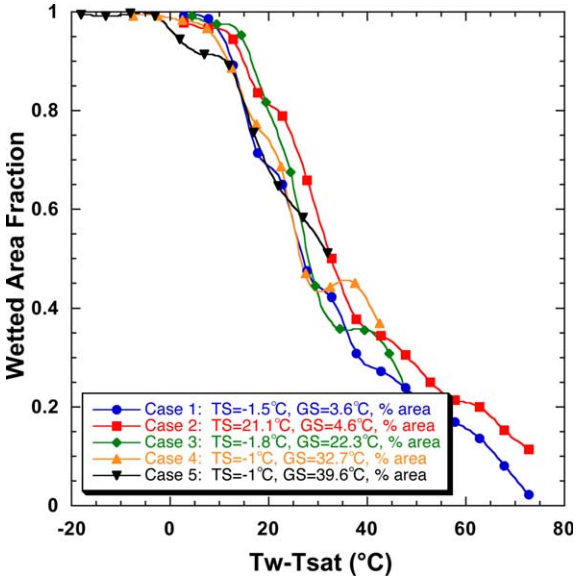

Fig. 11. Plots of the wetted area fraction as a function of wall superheat of the center eight heaters outlined in Fig. 1.

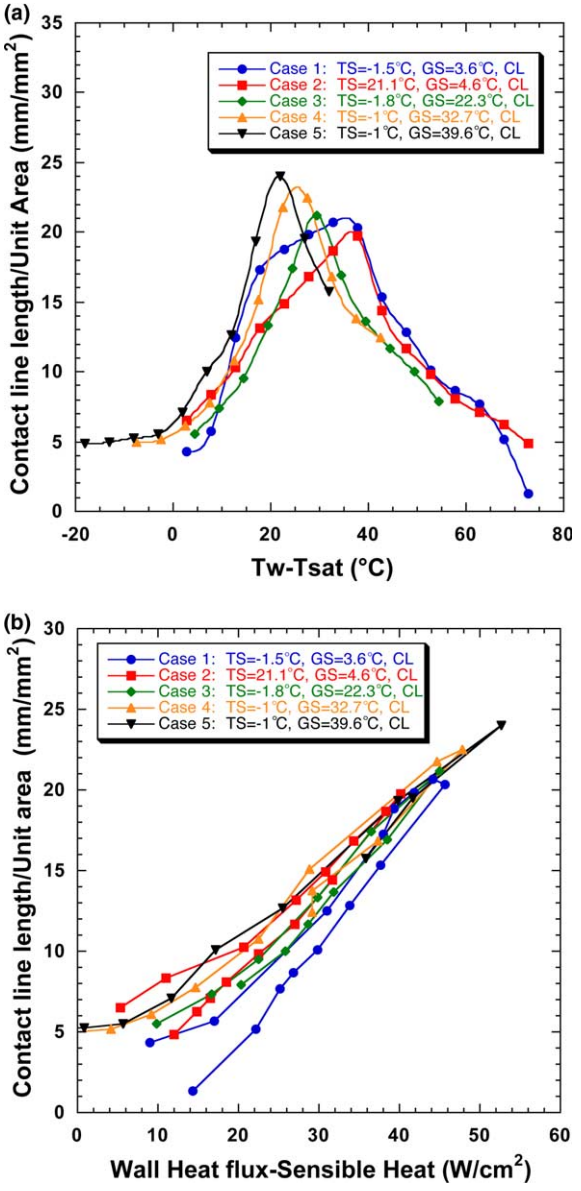

Fig. 12. Plots of the average contact line length for the center eight heaters outlined in Fig. 1 as a function of (a) the wall superheat, (b) the wall heat flux corrected for sensible heating.

highly gas-subcooled conditions (Case 5, $T_{w,CHF} - T_{sat} = 21.9$ °C).

The variation in CLL with wall superheat and heat flux is shown in Fig. 12. The data indicate that CLL increases with superheat (Fig. 12a), reaches a maximum at the superheat where CHF occurs, then decreases as the surface dries out. The curves' shapes are very similar to the heat flux profiles shown in Fig. 8, indicating a strong correlation between CLL and heat transfer. The relationship becomes clearer when CLL is plotted against heat flux (this has been corrected for sensible heating in a similar manner to the data in Fig. 8) as shown in Fig. 12b. CHF occurs at the highest CLL density. Increasing S_{tot} generally results in higher maximum values of CLL. The similarity in the CLL and heat flux curves indicates that the phase-change contribution to heat transfer is directly proportional to the CLL. It is unknown at this time whether heat is transferred at the contact line by the thin film heat transfer mechanisms suggested by Wayner [17] or by an alternate mechanism such as transient conduction into the liquid as it moves over the surface as has been proposed for pool boiling [18,19]. Further experiments which directly manipulate the contact line length in both a static and dynamic configuration are needed to elucidate which of these mechanisms might be responsible.

In summary, Figs. 11 and 12 indicate that as S_{tot} increases, CHF occurs at significantly larger wetted fractions (an increase of 70%) and slightly longer CLL (20%). This is consistent with fewer, larger droplets as S_{tot} increases. CHF does not appear to be caused by a deficit of liquid flux to the surface, but by the decreasing contact line as the wall superheat increases.

7. Conclusions

Wall heat transfer during spray cooling was measured using a microheater array, and the liquid vapor interface was visualized using a total internal reflection technique. The measurements indicated that the presence of non-condensible gas caused a shift in the saturation temperature of the liquid and increased the subcooling of the liquid being sprayed onto the surface. Gas effects on CHF could be accounted for using an existing correlation. For the conditions tested, the wall heat flux did not depend on the wetted area fraction of liquid on the surface, but correlated very well with the contact line length. The implications of this conclusion are that it may be possible to improve the control and magnitude of the heat flux if one can similarly enhance and/or control the contact line length on the heated surface. Future areas of investigation for this topic include constructing surfaces which influence the position of the contact line either through geometric structuring of the surface, or through manufacturing patterned surface coatings that selectively modify the local wetting of the surface.

Acknowledgments

This work was primarily supported by the Laboratory for Physical Sciences (LPS), College Park, MD under Grant No. MDA90499C2618. Additional funding was provided by the Air Force Research Laboratory (AFRL), Wright Patterson Air Force Base, Dayton, OH under Grant F33615-98-1-2791. The authors wish to express their gratitude to P. Boudreaux (LPS) and R. Ponnappan (AFRL) for their encouragement and support throughout this study.

References

[1] M.R. Pais, L.C. Chow, E.T. Mahefkey, Surface roughness and its effects on the heat transfer mechanism in spray cooling, J. Heat Transfer 114 (1992) 211–219.
[2] D.P. Rini, R.H. Chen, L.C. Chow, Bubble behavior and nucleate boiling heat transfer in saturated FC-72 spray cooling, J. Heat Transfer 124 (1) (2002) 63–72.
[3] J. Yang, L.C. Chow, M.R. Pais, Nucleate boiling heat transfer in spray cooling, J. Heat Transfer 118 (1996) 668–671.
[4] D.E. Tilton, C.L. Tilton, M.R. Pais, M.J. Morgan, High-flux spray cooling in a simulated multichip module, in: Proceedings of the 1992 ASME Heat Transfer Conference, HTD-Vol. 206-2, 1992.
[5] L. Lin, R. Ponnappan, Heat transfer characteristics of spray cooling in a closed loop, Int. J. Heat Mass Transfer 46 (2003) 3737–3746.
[6] S. Cui, S. Chandra, S. McCahan, Enhanced boiling of water droplets containing dissolved gases or solids, in: National Heat Transfer Conference, Pittsburgh, Pennsylvania, 2000, Paper No. NHTC 2000-12249.
[7] J. Lee, K.T. Kiger, J. Kim, Enhancement of droplet heat transfer using dissolved gases, SAE 2002 Trans. J. Aerospace (2002) 736–746.
[8] A. Frohn, N. Roth, Dynamics of Droplets, Springer-Verlag, Berlin, 2000.
[9] S. Nishio, T. Gotoh, N. Nagai, Observation of boiling structures near critical heat flux, in: M. Lehner, F. Mayinger (Eds.), Convective Flow and Pool Boiling, Taylor and Francis, 1999.
[10] S. Nishio, H. Tanaka, Visualization of boiling structures in high heat-flux pool-boiling'', Int. J. Heat Mass Transfer 47 (2004) 4559–4568.
[11] 3M Fluorinert Liquids Manual.
[12] K.N. Rainey, S.M. You, S. Lee, Effect of pressure, subcooling, and dissolved gas on pool boiling heat transfer from microporous surfaces in FC-72, J. Heat Transfer 125 (2003) 75–83.
[13] K.A. Estes, I. Mudawar, Correlation of sauter mean diameter and critical heat flux for spray cooling of small surfaces, Int. J. Heat Mass Transfer 38 (16) (1995) 2985–2996.

[14] I.A. Kopchikov, G.I. Voronin, T.A. Kolach, D.A. Labuntsov, P.D. Lebedev, Liquid boiling in a thin film, Int. J. Heat Mass Transfer 12 (1967) 791–796.
[15] S. Cui, S. Chandra, S. McCahan, The effects of dissolving salts in water sprays used for quenching a hot surface: Part 2—spray cooling, J. Heat Transfer 125 (2003) 333–338.
[16] I. Mudawar, K.A. Estes, Optimizing and predicting CHF in spray cooling of a square surface, J. Heat Transfer 118 (1996) 672–679.
[17] P. Wayner, Long range intermolecular forces in change of phase heat transfer (1998 Donald Q. Kern Award Review), in: ASME/AICHE National Heat Transfer Conference Paper #320, Albuquerque, NM, August 15–17, 1999.
[18] F. Demiray, J. Kim, Microscale heat transfer measurements during pool boiling of FC-72: effect of subcooling, Int. J. Heat Mass Transfer 47 (2004) 3257–3268.
[19] J.G. Myers, V.K. Yerramilli, S.W. Hussey, G.F. Yee, J. Kim, Time and space resolved wall temperature and heat flux measurements during nucleate boiling with constant heat flux boundary conditions, Int. J. Heat Mass Transfer, in press.